JOURNAL OF MATERIALS SCIENCE **33** (1998) 5069–5077

Precipitations in an yttrium-containing low-expansion superalloy

R. M. WANG*‡§, Y. F. HAN*, C. Z. LI*‡§, S. W. ZHANG*, D. H. PING‡, M. G. YAN*
*Beijing Institute of Aeronautical Materials, Beijing 100095, People's Republic of China
‡Laboratory of Atomic Imaging of Solids, Institute of Metal Research, Chinese Academy of Sciences, Shenyang 110015, People's Republic of China
§Beijing Laboratory of Electron Microscopy, Chinese Academy of Sciences, Beijing 100080, People's Republic of China
E-mail: rmwang@ihw.com.cn or biamqbjs@public3.bta.net.cn

The resistance to stress-accelerated grain-boundary oxygen embrittlement and notch-bar rupture strength in Fe–Ni–Co–Nb–Ti low-expansion superalloy has been improved significantly by trace yttrium addition. The precipitates in the matrix as well as along the grain boundaries have been studied systematically. The platelet precipitates in the matrix and along the grain boundaries have a hexagonal crystal structure (space group, $P6/mmm$) with lattice parameters $a = 0.498$ nm and $c = 0.408$ nm. The crystallographic orientation relationship between the phase and the matrix is found to be $(\bar{1}\,\bar{1}\,1)_\gamma // (0\,0\,0\,1)_H$, $[\bar{1}\,1\,0]_\gamma // [1\,1\,\bar{2}\,0]_H$. The semi-continuous discrete precipitates along the grain boundaries have an orthorhombic crystal structure with lattice parameters $a = 0.45$ nm, $b = 0.80$ nm and $c = 1.20$ nm. High-resolution images show that the interface between the precipitates and the matrix is semicoherent.

1. Introduction

Chromium-free low-coefficient-of-thermal-expansion (CTE) alloys based on the system Fe–Ni–Co–Nb–Ti are attractive for aerospace and land-based gas turbine engine applications, because they can reduce the clearance necessary between the turbine blade tips and the retainer, simplifying the design and substantially improving the fuel efficiency [1–3]. The most important question in the alloys is the susceptibility of these alloys to stress-accelerated grain-boundary oxygen embrittlement (SAGBO) due to the absence of chromium [4, 5]. Smith and co-workers [4, 5] found that the platelet precipitation along the grain boundaries can improve the resistance to SAGBO at elevated temperatures in Incoloy alloy 909. Many efforts, such as adding some antioxidant element, or modifying the heat treatment, have been made to improve the SAGBO resistance and the notch-bar rupture strength, but it will cause some other problems. For example, the CTE of the alloy will be increased with 1–2 wt% Cr addition. One possible way to improve the resistance to SAGBO is to add trace rare-earth elements during the processing. However, the influence of the rare-earth elements on the properties and microstructures of the low-expansion superalloy has not been reported. Many studies on the rare-earth element effects on steel and aluminium alloys have been made. Lu and Xu [6] proposed that the rare earth elements segregate at the grain boundaries and refine the Martanize grain size in low alloying steel. Lin [7] studied Al–Zn–Mg alloy and found that the strengthening precipitates were refined and denser on rare-earth element addition. In the Incoloy alloy series, there was some controversy on the crystal structure of the platelet precipitates. Heck *et al.* [5] suggested the phase to be $D0_{19}$ type by means of X-ray diffraction. On the other hand, Chen [8] suggested it to be orthorhombic by means of selected-area electron diffraction (SAD) and convergent-beam electron diffraction (CBED). We [9, 10] have also investigated the phases precipitated along the grain boundaries of the Fe–Ni–Co–Nb–Ti low-expansion superalloy. In this paper, the microstructure of the platelet or rod-like precipitates and the discrete precipitate phases in the yttrium-containing low-expansion superalloy are investigated systematically by transmission electron microscopy, CBED, high-resolution transmission electron microscopy (HREM) and energy-dispersive X-ray analysis (EDXA).

2. Experimental procedure

The chemical composition of the low-expansion superalloy is given in Table I.

The samples were solution treated at 1120 °C for 24 h in vacuum and then aged at 980 °C for 1 h. 775 °C for 12 h and 620 °C for 8 h. The cooling rate was 55 °C h^{-1}.

Specimens for transmission electron microscopy (TEM) were cross-sectioned and polished to a thickness of 30–50 μm. The final finishing was achieved by twin-jet electrolytic polishing followed by a short ion milling. The electrolytic solution was 10% perchloric

TABLE I Chemical composition of the yttrium-continuing low-expansion superalloy

Element	Ni	Co	Nb	Ti	Al	Si	Y	Fe
Amount (wt %)	38.14	13.38	4.52	1.40	0.11	0.17	<0.1	Balance

acid in ethanol at a voltage of about 90 V and a temperature of −20 °C or below. The ion miller was a Gatan 600 at a voltage of 4.5 kV and an incident angle of 10°.

Conventional TEM analysis was performed on an H-800 transmission electron microscope operated at 200 kV. The device for EDXA (scanning transmission electron microscopy mode) was a TN5500 equipped with a diamond window detector. The software was a SQ Tracter Northern Series II system. HREM images were obtained on JEOI, 2000EX II and JEOI, 2010 microscopes at 200 kV. Specimens for CBED were prepared as carbon extraction replicas. The CBED was performed on an EM-420 operated at 100 kV and an EM12 operated at 120 kV. The software for SAD pattern analysis and the determination of the crystallographic orientation relationship between the two phases was set up by Li and Yan [11].

3. Results and discussion

The yttrium-containing low-expansion superalloy has an excellent combination of tensile properties, notch rupture strength and low thermal expansion. Investigations have shown that yttrium has little effect on the tensile strength. However, it had a dramatic effect on the notch-bar rupture life at 540 °C and 825 MPa [12]. The notch-bar rupture life increased to 185–225 h on trace yttrium addition. The good resistance to SAGBO is probably due to the precipitates of the platelet phase [5].

On ageing after solution treatment at 1120 °C, precipitates with a platelet morphology formed in the matrix as well as along the grain boundaries. Fig. 1 is a typical optical microstructure of the investigated alloy and shows massive platelet precipitates. Fig. 2 shows the $[1\,1\,0]_\gamma$ direction bright-field image of the platelet precipitates where γ indicates the matrix. Two sections of the platelet phase were observed. The slender section is about 50 nm in size and the broad section is about 200 nm in size. In Fig. 2, the direction of the platelet phase are $[0\,0\,0\,1]_H$ and $[1\,1\,0\,0]_H$.

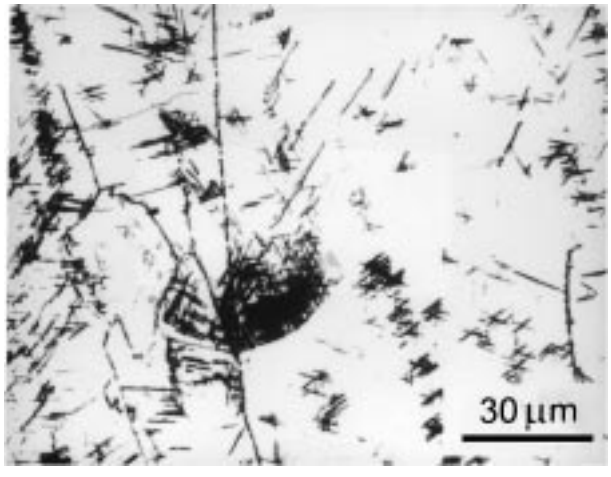

Figure 1 Typical optical microstructure of the alloy investigated showing massive platelet precipitates.

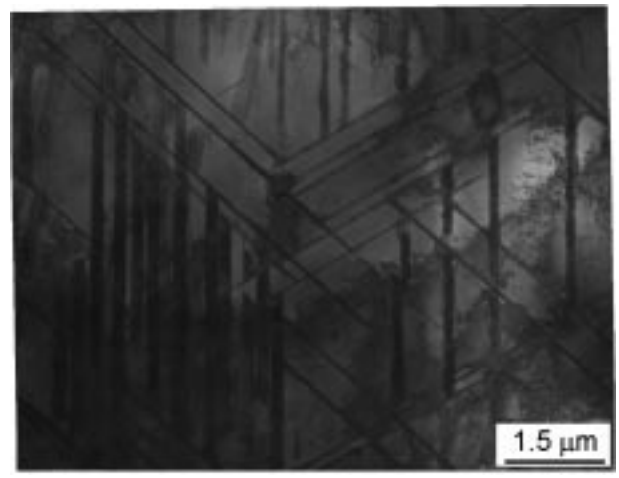

Figure 2 $[1\,1\,0]_\gamma$ direction bright-field image of the platelet precipitates in the matrix.

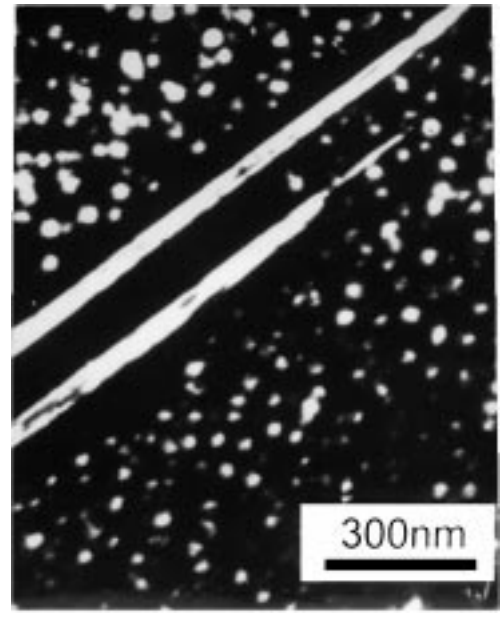

Figure 3 (1 1 2 0) reflection dark-field image of the platelet phase in the matrix.

Fig. 3 is a (1 1 2 0) reflection dark-field image of the platelet phase in the matrix. The major strengthening constituent precipitates, i.e., γ' phase, are also observed. The γ' particles are mostly squared or spherical with a size of 20–40 nm.

Fig. 4 shows a $[1\ 1\ 0]_\gamma$ bright-field image of the platelet phase along the grain boundaries. The precipitates are rod like about 1 μm long and 10 nm in diameter. Compared with those in the matrix, the platelet precipitates along the grain boundaries are shorter but thicker. In other words, the morphologies of the platelet phase precipitates observed in the microscope are needle like or rod like of different sizes.

Since the mechanism of formation of the grain-boundary phase is rather complex, various phases appear to precipitate along the grain boundaries. As well

TABLE II EDX results of the precipitates and platelet phase in yttrium-containing superalloy where the Error is within parenthesis

Element	Fe	Ni	Co	Nb	Ti	Al	St
Amount in platelet	26.12(1.5)	42.76(2.5)	13.02(1.0)	14.67(0.5)	2.15(0.2)	0.25(0.1)	1.03(0.1)
Amount in lumpy precipitation	28.97(2.0)	32.30(2.0)	13.86(1.5)	22.92(1.5)	1.88(0.2)	-	

as the platelet phase, a kind of semi-continuous discrete precipitate was observed along the grain boundaries, as shown in Fig. 5. Investigations indicate that the crystal structure and chemical composition are different from those of the platelet precipitates.

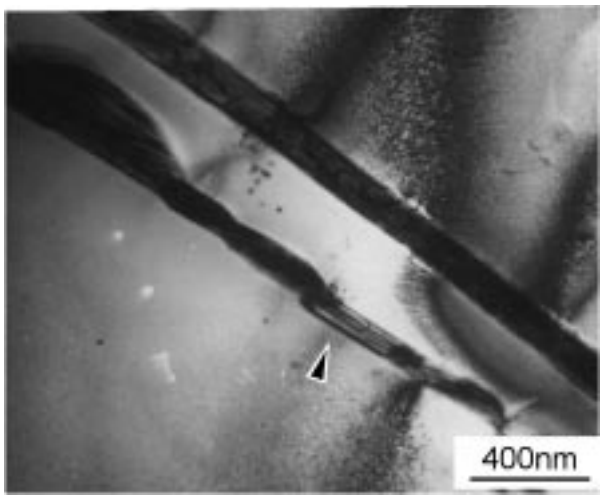

Figure 4 Bright-field image of the platelet phase along grain boundaries.

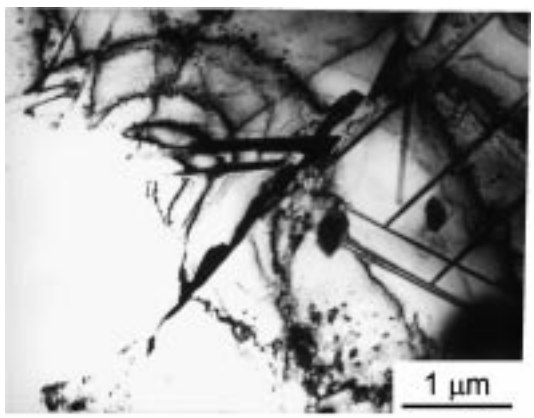

Figure 5 Bright-field image of the semi-continuous discrete precipitates along grain boundaries.

Fig. 6a is the energy-dispersive X-ray spectrum from the platelet phase. Many spots, including the rod-like precipitates along the grain boundaries, have been detected. The spot size ranges from 20 to 100 nm according to the size of the precipitates. No significant difference between the chemical compositions of the precipitates was found. The results are summarized in Table II. The values of the errors are also presented in Table II, in parentheses. Then the molecular formula of the platelet or rod-like phase may be written as (Fe, Ni, Co)$_5$(Nb, Ti, Al, Si). However, investigations indicate that the chemical composition of the semicontinuous discrete phase is different from that of the platelet phase. Fig. 6b shows the energy-dispersive X-ray spectrum from the discrete lumpy phase. The results are also summarized in Table II. The Nb content of the lumpy phase is much higher than that of the platelet phase. Another difference is that there is almost no Si in the lumpy phase. The molecular formula may be written as (Fe, Ni, Co)$_3$(Nb, Ti), which is consistent with the results of Heck *et al.* [5] and Chen [8].

Fig. 7 shows the SAD and indexed patterns and the corresponding CBED patterns for various zone axes from the platelet phase. Fig. 7a shows a SAD and indexed patterns related to [0 0 0 1] zone axis of the phase. The corresponding CBED pattern is shown in Fig. 7b. The CBED pattern in Fig. 7b show 6 *mm* symmetry, which corresponds to the diffraction groups 3 $m1_R$, $6m_Rm_R$, 6 *mm* or $6mm1_R$ and the point groups 6*m*2, 622, 6*mm* or 6/*mmm*. Fig. 7c and d are the SAD and CBED patterns, respectively, related to the [1 1 0 0] zone axis. The CBED pattern symmetry is 2*mm*, corresponding to the diffraction groups 2*mm* or $2\underline{m}\underline{m}1_R$ and the point groups 6/*mmm* or 6*m*2. For the [1 1 2 0] zone axis as shown in Fig. 7e and f, the CBED pattern symmetry is also 2*mm*, which corresponds to the diffraction groups 2*mm* or $2mm1_R$ and the point group 6/*mmm*. The results are listed in Table III. From Table III it may be concluded that the point group of the platelet phase is 6/*mmm*. More experiments have shown that the platelet phases along the grain boundaries have the same crystal structure as those in the matrix.

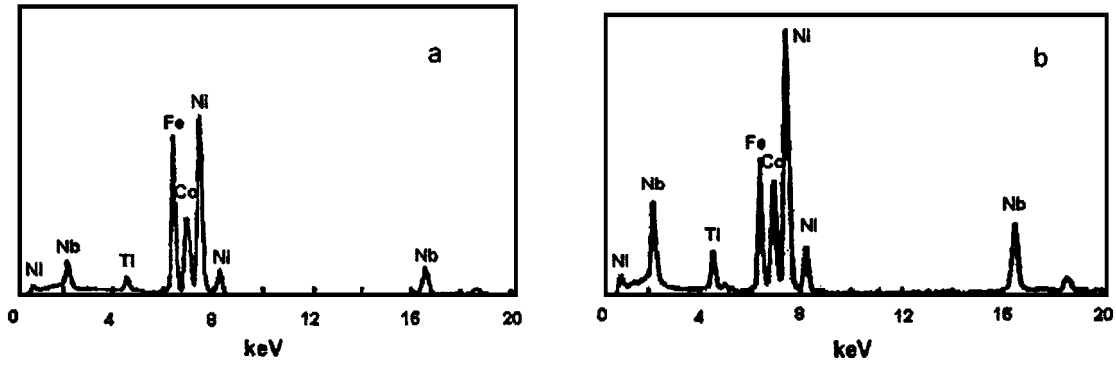

Figure 6 Energy-dispersive X-ray spectrum from the precipitates of the yttrium-containing low-expansion superalloy:(a) platelet precipitate: (b) discrete lumpy precipitate.

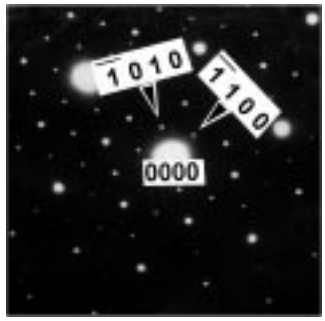

(a)

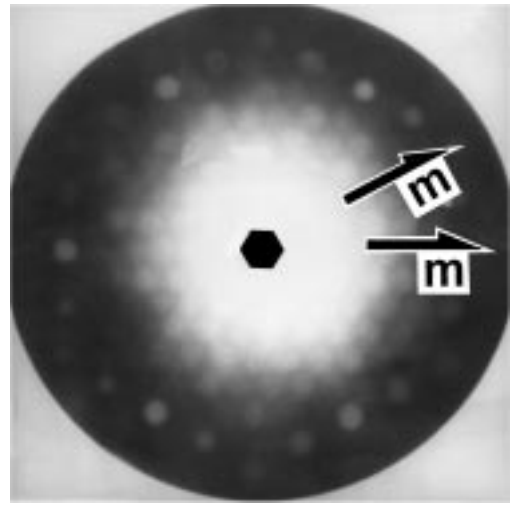

(b)

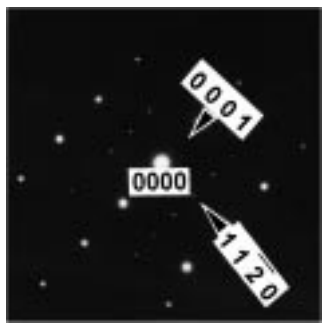

(c)

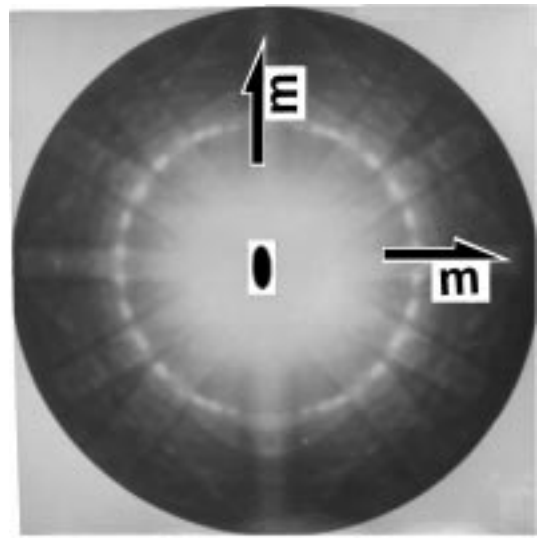

(d)

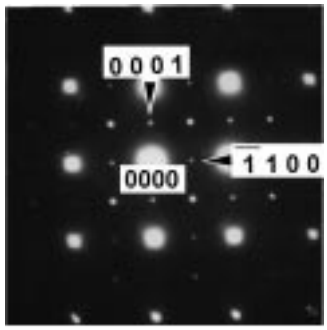

(e)

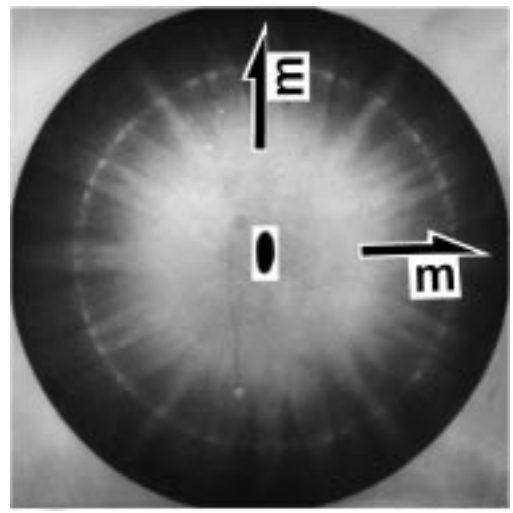

(f)

Figure 7 (a) $[0\ 0\ 0\ 1]_H$, (c) $[1\ 1\ 0\ 0]_H$ and (e) $[1\ 1\ 2\ 0]_H$ SAD patterns and (b), (d), (f) to corresponding CBED patterns from the platelet phase showing 6*mm*, 2*mm* and 2*mm* symmetry, respectively.

The possible space groups corresponding to the point group $6/mmm$ include $P6/mmm$, $P6/mcc$, $P6_3/mcm$ and $P6_3/mmc$. As no Gjønnes-Moudle [13] line can be found in the diffraction plates, the space group of the H phase is probably not $P6/mcc$ nor $P6_3/mcm$ nor $P6_3/mmc$. Thus the space group of the H phase is $P6/mmm$.

From the SAD patterns of the $[0\ 0\ 0\ 1]_H$ and $[1\ \bar{1}\ 0\ 0]_H$ zone axes of the platelet phases both in the matrix and along the grain boundaries, the lattice

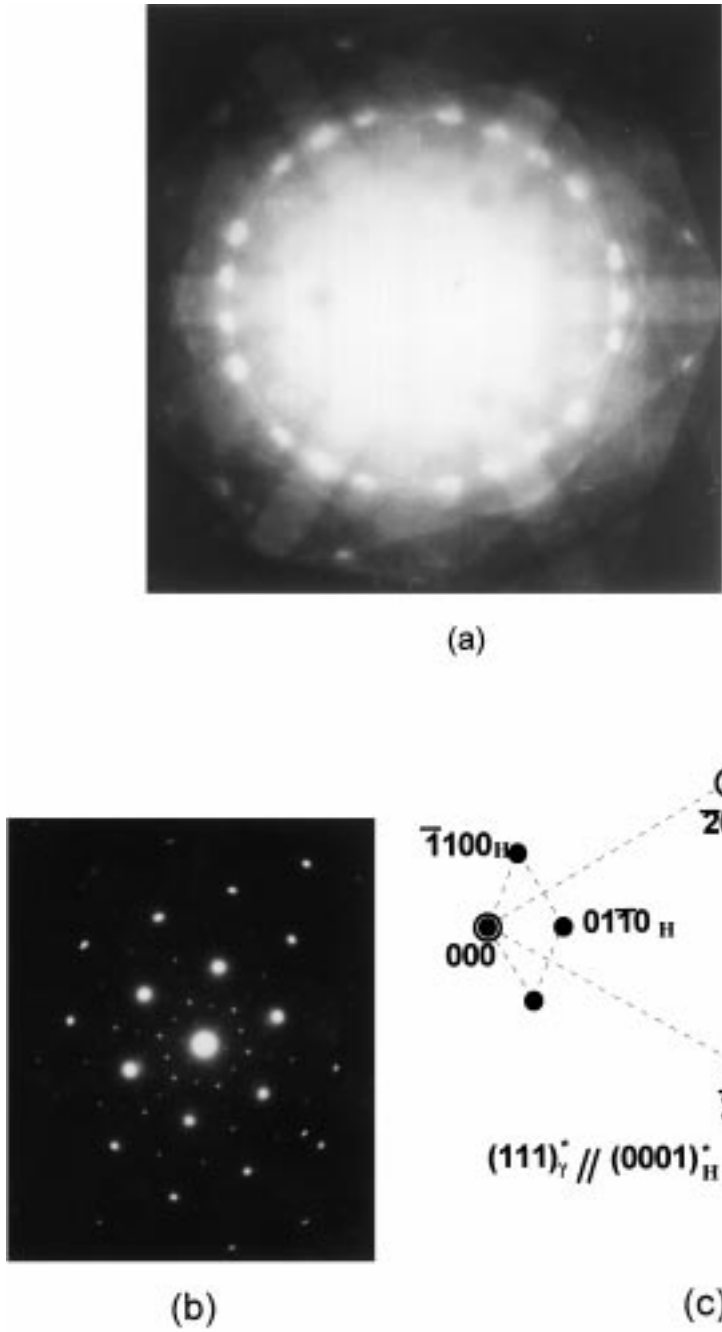

Figure 8 $[1\,1\,1]_\gamma$ and $[0\,0\,0\,1]_H$ (a) complex CBED, (b) SAD and (c) indexed patterns from the H phase and the matrix.

TABLE III The determination of the point group of the platelet phase

Zone	CBED pattern symmetry	Possible diffraction groups	Possible point groups
[0 0 0 1]	6*mm*	$3ml_R$,$6m_R\,m_R$, 6*mm*, $6mml_R$	$\bar{6}m2$, $62\bar{2}$, 6*mm*, $\bar{6}mmm$
$[1\bar{1}00]$	2*mm*	2*mm*, $2mml_R$	6/*mmm*, 6*m*2
$[1\bar{1}01]$	2*mm*	2*mm*, $2mml_R$	6/*mmm*

parameters of the H phase are obtained to be $a = 0.498$ nm and $c = 0.408$ nm. The camera constant was internally calibrated since the lattice parameters of the matrix are known.

Fig. 8 gives a complex CBED pattern and corresponding SAD and indexed patterns from both the H phase and the matrix γ phase. The matrix γ phase has a face-centred cubic crystal structure with $a = 0.3608$ nm. From the complex CBED and SAD patterns, it can be seen that the H phase and the γ phase exhibit a definite orientation relationship.

In Fig. 8a, the incident beam is parallel to $[1\,1\,1]_\gamma$. The CBED symmetry of the matrix along the [1 1 1] zone axis is 3*m* and the CBED symmetry of the H phase along the [0 0 0 1] zone axis is 6*mm*. The 3*m* symmetry of the complex CBED pattern indicates that $[0\,0\,0\,1]_H$ is exactly parallel to [1 1 1]. The corresponding SAD pattern also confirms the orientation relationship.

Fig. 8b indicates that $(\bar{2}\,0\,2)_\gamma // (1\,\bar{2}\,1\,0)_H$, $[1\,1\,1]_\gamma // [0\,0\,0\,1]_H$. According to the method in [1 1] for

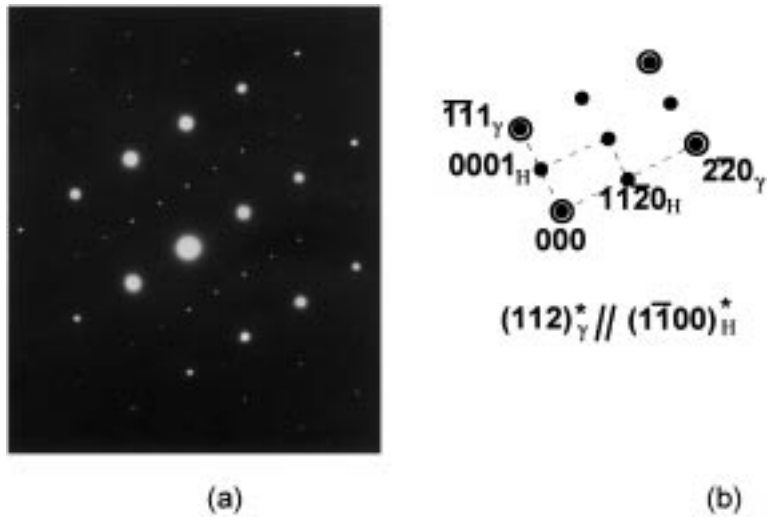

Figure 9 $[1\,1\,2]_\gamma$ and $[1\,1\,2\,0]_H$ (a) complex SAD and (b) indexed patterns from the H phase and the matrix.

determination of the orientation relationship between the two phases and consideration of the 180° ambiguity, the corresponding transformation matrix of the direction indices is:

$$B_1 = \begin{bmatrix} -0.342 & 0.683 & -0.342 \\ -0.683 & 0.342 & 0.342 \\ 0.511 & 0.511 & 0.511 \end{bmatrix}$$

Fig. 9 gives another complex SAD pattern of both the H phase and the matrix. Fig. 9a indicates that $(1\,1\,1)_\gamma // (0\,0\,0\,1)_H$, $[1\,1\,2]_\gamma // [1\,1\,0\,0]_H$. The corresponding transformation matrix of the direction indices is:

$$B_2 = \begin{bmatrix} -0.342 & 0.683 & 0.342 \\ -0.683 & 0.342 & -0.342 \\ -0.511 & -0.511 & 0.511 \end{bmatrix}$$

From the equivalent matrices B_1 and B_2, it may be suggested that the two orientation relationships $(1\,\bar{1}\,1)_\gamma // (0\,0\,0\,1)_H$, $[1\,1\,\bar{2}]_\gamma // [1\,\bar{1}\,0\,0]_H$ and $(\bar{2}\,0\,2)_\gamma // (1\,2\,\bar{1}\,0)_H$, $[1\,1\,1]_\gamma // [0\,0\,0\,1]_H$ are equivalent. More complex SAD patterns from the H phase and the matrix show that all transformation matrix of direction indices are equivalent [12]. From the matrix B_1, we can obtain a typical crystallographic orientation relationship $(1\,1\,1)_\gamma // (0\,0\,0\,1)_H$, $[1\,1\,0]_\gamma // (1\,1\,2\,0]_H$ which indicates that the closed planes and directions of the two phases are parallel to each other. Then the diagram of crystallographic orientation relationship between the H phase and the matrix can be obtained, as shown in Fig. 10 where $\boldsymbol{a}, \boldsymbol{b}$ and $\boldsymbol{c}$ are the unit vectors of the matrix while $\boldsymbol{a}'$, $\boldsymbol{b}'$ and $\boldsymbol{c}'$ are the unit vectors of the H phase.

The relationship between the unit vectors of the H phase and the matrix is as follows:

$$\begin{aligned} \boldsymbol{a}' &= \boldsymbol{b} + \boldsymbol{c} \\ \boldsymbol{b}' &= \boldsymbol{a} - \boldsymbol{c} \\ \boldsymbol{c}' &= 2(-\boldsymbol{a} - \boldsymbol{b} + \boldsymbol{c})/3 \end{aligned}$$

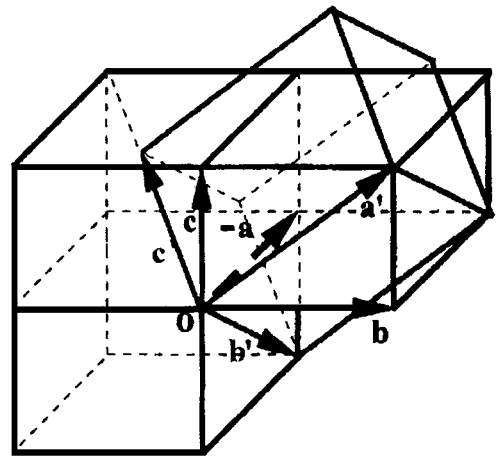

Figure 10 Diagram of the crystallographic orientation relationship between the H phase and the matrix **a**, **b**, **c** and the unit vectors of the matrix; $\mathbf{a}'$, $\mathbf{b}'$, and $\mathbf{c}'$ are the unit vectors of the H phase.

Then $\boldsymbol{d}' = -(\boldsymbol{a}' + \boldsymbol{b}') = \boldsymbol{a} - \boldsymbol{b}$. If we reverse the vectors of $\boldsymbol{a}$ and $\boldsymbol{b}$, then

$$\begin{aligned} \boldsymbol{a}' &= \boldsymbol{b} - \boldsymbol{c} \\ \boldsymbol{b}' &= \boldsymbol{a} - \boldsymbol{c} \\ \boldsymbol{c}' &= 2(\boldsymbol{a} + \boldsymbol{b} + \boldsymbol{c})/3 \\ \boldsymbol{d}' &= -\boldsymbol{a} + \boldsymbol{b} \end{aligned}$$

Then the equation $-\boldsymbol{a}' + 2\boldsymbol{b}' - \boldsymbol{d}' = -3(-\boldsymbol{a} + \boldsymbol{c})$ can be obtained which indicates that the $(1\,2\,\bar{1}\,0)$ planes of the H phase is parallel to the $(\bar{1}\,0\,1)$ planes of the matrix. The equation $\boldsymbol{c}' = 2(\boldsymbol{a} + \boldsymbol{b} + \boldsymbol{c})/3$ indicates that the $[0\,0\,0\,1]$ direction of the H phase is parallel to the $[1\,1\,\bar{1}]$ direction of the matrix. From these it may be concluded that Fig. 10 also represents the orientation relationship of matrix $\boldsymbol{B}_2$.

Investigations indicate that the lumpy phase along the grain boundaries is the orthorhombic phase identified by Chen [8]. The point group is *mmm* with lattice parameters $\boldsymbol{a} = 0.45$ nm, $\boldsymbol{b} = 0.80$ nm and $\boldsymbol{c} = 1.20$ nm. In this paper, we describe it as the O phase. Fig. 11 shows a HREM image of the O phase and the matrix.

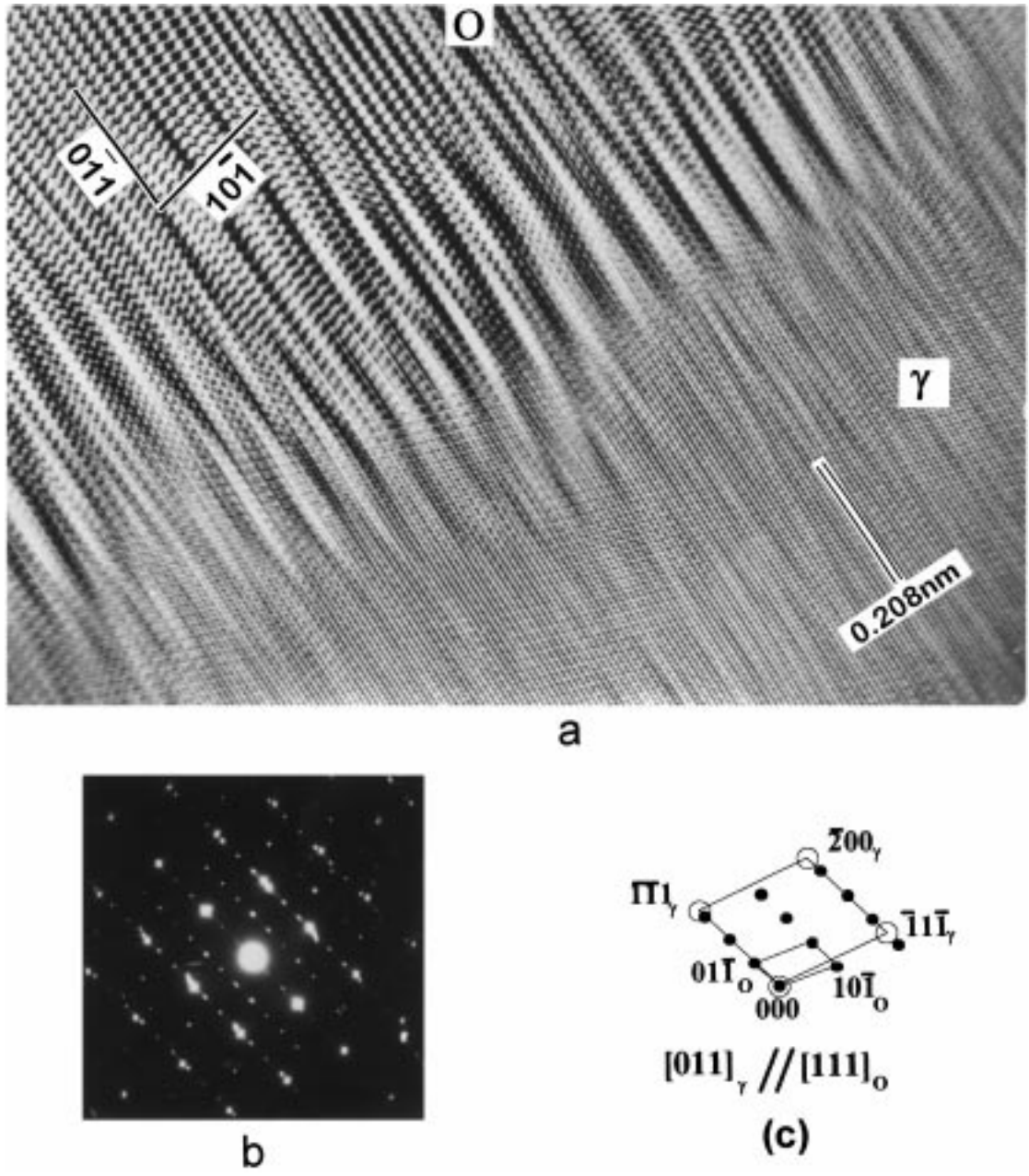

Figure 11 (a) HREM image of the O phase and the matrix (b) the corresponding SAD pattern and (c) the indexed pattern.

Fig. 11b and c are the corresponding SAD and indexed patterns, respectively. The small full circles represent the reflections from the H phase and the open circles represent those from the matrix. The incident beam is parallel to $[1\,1\,1]_O//[1\,1\,0]$. The interface is clean and smooth but not straight. No reaction product was found at the interface. The interplanar distances of (0 1 1) and (1 0 1) planes in the O phase are 0.666 nm and 0.421 nm, respectively, and that of (1 1 1) plane in the matrix is 0.208 nm.

In most cases, no reaction take place at the interface between the O phase and the matrix, but sometimes a Laves phase about a few nanometers in size has been found at the interface [9].

Fig. 12a is a HREM image of the H phase in the matrix. Fig. 12b and c are corresponding SAD and indexed patterns, respectively. The small full circles represent the reflections from the H phase and the open circles represent those from the matrix. The incident beam is parallel to $[1\,2\,\bar{1}\,0]_H//[0\,1\,1]$ and the interface is parallel to $(0\,0\,0\,1)_H//(1\,1\,1)_\gamma$. The interface, as indicated by a double arrowhead in Fig. 12a, is very clean, smooth and straight. No reaction product has been found at the interface. The interplanar spacings of the (0 0 0 1) plane and the (1 1 0 0) plane in the H phase are 0.408 nm and 0.431 nm, respectively. The atomic spacings of $(0\,0\,0\,1)_H$ and $(1\,1\,1)_\gamma$ are 0.431 nm and 0.221 nm, respectively, which gives a semicoherent interface where every two $(1\,1\,1)_\gamma$ atoms correspond to one $(0\,0\,0\,1)_H$ atom group with a mismatch of about 1%. Some stacking faults can also be found in the $(0\,0\,0\,1)_H$ phase, as indicated in Fig. 12a. On the SAD pattern, the weak reflections besides those of the H phase represent the faults. The stacking faults also make it difficult to obtain a high-quality CBED pattern from the H phase. Investigation indicates that the interface between the intergranular H phase and the

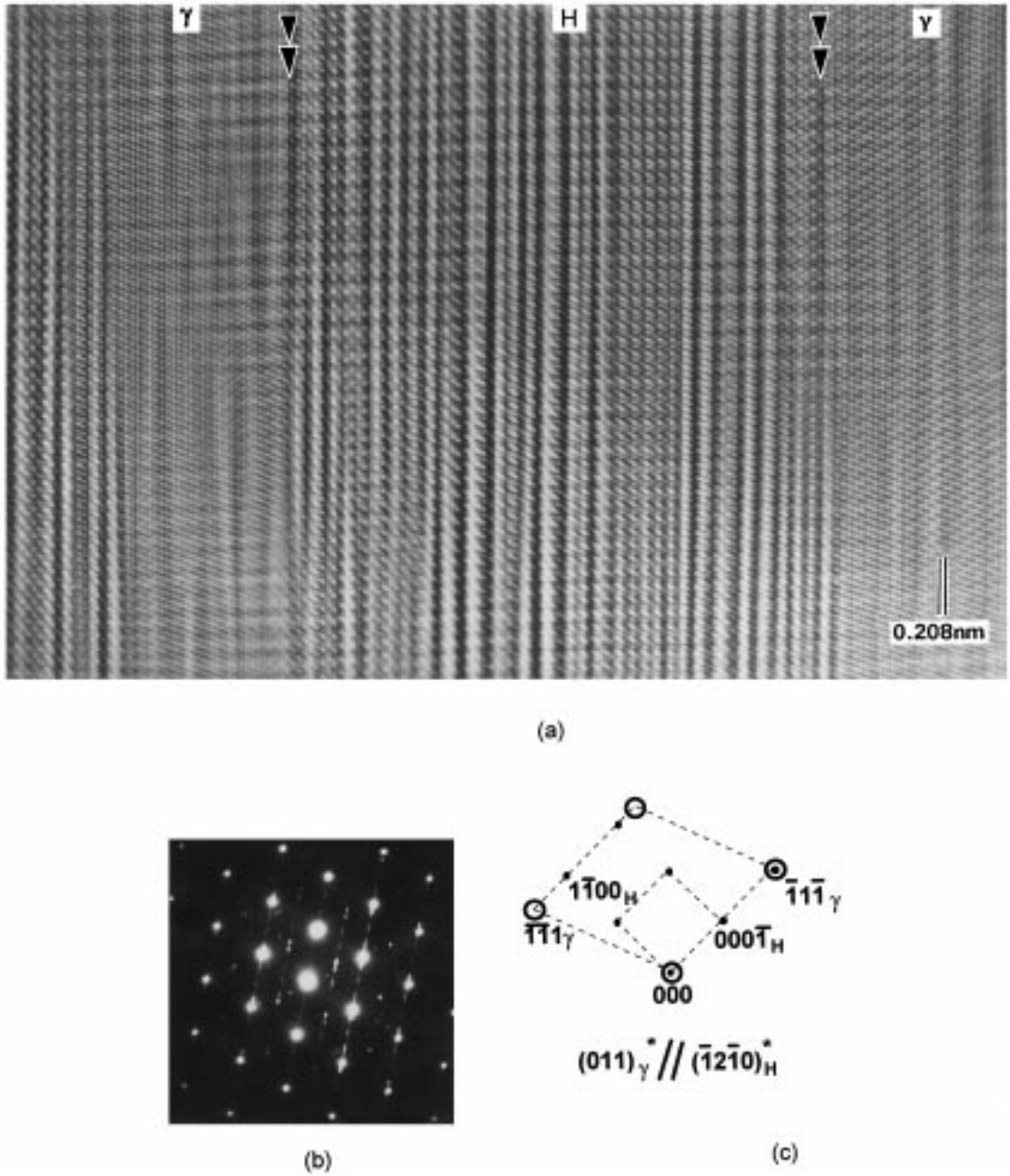

Figure 12 (a) HREM image of the H phase in the matrix (b) the corresponding SAD pattern and (c) the indexed pattern.

matrix is also clean, smooth and straight, just as that of the interface between the intragranular H phase and the matrix [10].

4. Conclusions

1. The platelet and rod-like precipitate phase in the yttrium-containing Ni–Fe–Co–Nb–Ti low-expansion superalloy is the H phase. The point group is $6/mmm$ with lattice parameters $a = 0.498$ nm and $c = 0.408$ nm. The space group is $P6/mmm$ and the composition may be written as $(Fe, Ni, Co)_5(Nb, Ti, Al, Si)$.

2. The orientation relationship between the H phase and the matrix γ phase is $(1\,\bar{1}\,1)_\gamma // (0\,0\,1)_H$, $[1\,1\,0]_\gamma // [1\,1\,\bar{2}\,0]_H$.

3. The semicontinuous discrete phase along the grain boundaries in the alloy is the O phase with lattice parameters $a = 0.45$ nm, $b = 0.80$ nm and $c = 1.20$ nm. The chemical composition may be written as $(Fe, Ni, Co)_3(Nb, Ti)$.

Acknowledgements

The authors thank the Chinese Science Foundation of Aeronautics for supporting their research.

References

1. D. F. SMITH, E. F. CLASTWORTHY, D. G. TIPTON and W. L. MANKINS, *Superalloys* 1980 (American Society for Metals, Metals Park, OH, 1980) pp. 521–530.
2. M. M. MORRA, R. G. BALLINGER and J. S. HWANG, *Metall. Trans. A* **23** (1992) 3177.
3. K. SATO and T. OHNO, *J. Mater. Engng. Performance* **2** (1993) 511.
4. D. F. SMITH, J. S. SMITH and S. FLOREEN, in "Superalloys 1984," Proceedings of the Fifth International Symposium on

Superalloys, Seven Springs, PA (American Society for Metals, Metals Park, OH, 1984) pp. 591–600.
5. K. A. HECK, D. F. SMITH, J. S. SMITH, D. A. WELLS and M. A. HOLDERBY, *Superalloys* 1988, edited by S. Reichman, D. N. Duhl, G. Maurer, S. Antolovich and C. Lund (Metallurgical Society of AIME, Warrendale, PA, 1988) pp. 151–160.
6. W. LU and Z. Y. XU, *Acta Metall Sin.* **10** (1993) A307–311.
7. Z. Q. LIN, *Chin. J. Rare Earth Res.* **10** (1992) 247–252.
8. Z. CHEN, *Scripta Metall. Mater.* **26** (1992) 1077–1082.
9. R. M. WANG, C. Z. LI, S. W. ZHANG and M. G. YAN, *Acta Metall. Sin.* **9** (1996) 595.
10. R. M. WANG, C. Z. LI, J. T. YU and M. G. YAN, *Chin J. Aeronaut. Mater.* **15** (1995) 1.
11. C. Z. LI and M. G. YAN, *Chin. J. Metal. Sci. Technol.* **3** (1987) 27.
12. R. M. WANG, C. Z. LI, S. W. ZHANG and M. G. YAN. unpublished.
13. J. GJØNNES, A. F. MOODLI, *Acta Crystallogr.* **19** (1965) 65.

Received 12 March 1997
and accepted 5 February 1998